Terramechanics-based Model for Steering Maneuver of Planetary Exploration Rovers on Loose Soil

Genya Ishigami
Department of Aerospace Engineering
Tohoku University
Aoba 6-6-01, Sendai, 980-8579, JAPAN
ishigami@astro.mech.tohoku.ac.jp

Akiko Miwa
Department of Aerospace Engineering
Tohoku University
Aoba 6-6-01, Sendai, 980-8579, JAPAN
miwa@astro.mech.tohoku.ac.jp

Keiji Nagatani
Department of Aerospace Engineering
Tohoku University
Aoba 6-6-01, Sendai, 980-8579, JAPAN
keiji@astro.mech.tohoku.ac.jp

Kazuya Yoshida
Department of Aerospace Engineering
Tohoku University
Aoba 6-6-01, Sendai, 980-8579, JAPAN
yoshida@astro.mech.tohoku.ac.jp

Abstract

This paper presents analytical models to investigate the steering maneuvers of planetary exploration rovers on loose soil. The models are based on wheel-soil interaction mechanics, or terramechanics, with which the traction and disturbance forces of a wheel are evaluated for various slip conditions. These traction forces are decomposed into the longitudinal and lateral directions of the wheel. The latter component, termed the *side force* has a major influence in characterizing the steering maneuvers of the rover. In this paper, the wheel-soil mechanics models are developed with particular attention to the side force, and the validity of the model is confirmed by using a single-wheel test bed. The motion profile of the entire rover is numerically evaluated by incorporating the wheel-soil models into an articulated multibody model that describes the motion dynamics of the vehicle's body and chassis. Steering maneuvers are investigated under different steering angles by using a four-wheel rover test bed on simulated lunar soil (*regolith simulant*). The experimental results are compared with the simulation results using the corresponding model parameters. The proposed wheel-and-vehicle model demonstrates better accuracy in predicting steering maneuvers as compared to the conventional kinematics-based model.

1 Introduction

There have been an increasing number of space mission programs involving lunar/planetary exploration with regard to the quest for the origin of the solar system and future in-situ

resource utilization. The use of mobile robots, or *rovers*, in these missions significantly expands the exploration areas and thus increases the scientific or programmatic return from the mission. These planetary exploration rovers are expected to travel long distances and perform complex tasks in order to fulfill challenging mission goals.

The surface terrain of the Moon or a planet such as Mars is largely covered with a fine-grained loose soil called *regolith*. On such loose soil, the wheels of a rover easily slip and lose traction. Therefore, investigations on the contact and traction mechanics between the wheels and the soil are necessary in order to better understand the motion behavior of a rover on loose soil.

Wheel-soil interaction mechanics is included in the field of *terramechanics*. In this field, the principle of the wheel-soil interaction mechanics and the empirical models of the stress distributions beneath the wheels have been previously investigated (Bekker, 1960; Bekker, 1969; Wong, 1978). Recently, these terramechanics-based models have been successfully applied to the motion analysis of planetary rovers (Iagnemma and Dubowsky, 2004). A simulator considering terrain environments and terrain/vehicle interactions has been developed (Jain et al., 2003). A multibody system simulation for the longitudinal slip of tires with respect to a tire-soil interaction has also been demonstrated (Gibbesch and Schäfer, 2005). We have also developed a terramechanics-based dynamics model for exploration rovers by considering the slip and traction forces of a rigid wheel on loose soil (Yoshida and Hamano, 2002; Yoshida et al., 2003). Despite such intensive research regarding the traction mechanics of rover wheels, the steering characteristics of rovers have not been sufficiently analyzed. Understanding the steering maneuvers is necessary in order to predict the motion behavior of the rover on loose soil and also to discuss off-line path planning issues and the trajectory tracking controls of rovers.

In this paper, analytical models to investigate the steering maneuvers of planetary exploration rovers are addressed. The steering motion of the rovers on loose soil is dissimilar to that of on-road vehicles because of the different wheel slip/skid behaviors. This is the reason why conventional kinematics-based steering models for on-road vehicles are not applicable in these cases. To deal with motion dynamics, or even just a kinematic trace of a vehicle on loose soil, appropriate models for both wheel slip in the longitudinal direction and skid in the lateral direction are necessary. This research studies two models to address steering maneuvers. First, a wheel-soil contact model is developed to deal with the wheel slip/skid behaviors, and subsequently, the steering motion of the rover is numerically obtained by using a wheel-and-vehicle model.

As mentioned above, there are a number of studies pertaining to the traction mechanics of a rigid wheel on loose soil; however, most are focused on the longitudinal characteristics of the net traction force, the *drawbar pull*. There are, however, few studies that seriously investigate the lateral characteristics of a wheel on loose soil, which are indispensable in a discussion of the steering maneuvers of a vehicle. This research addresses the wheel traction models, including the lateral force, or the *side force*, while reviewing the basics of wheel-soil contact mechanics on loose soil. Here, the side force is decomposed into the shear force beneath the wheel and the bulldozing resistance force on the side face of the wheel; these two forces are then modeled analytically. Finally, the relationships among the slip ratio (a

measure of the longitudinal slip), slip angle (a measure of the lateral slip), drawbar pull, and side force are derived.

The validity of the wheel-soil contact model and the theoretical relationships is confirmed through experiments using a single-wheel test bed with different slip ratios and slip angles. The results show that the proposed wheel-soil contact model provides reasonable theoretical curves that agree with the corresponding experimental data with relatively good accuracy. In these experiments, *lunar regolith simulant* is utilized, which simulates the soil on the lunar surface. The key parameters of the soil and the wheel-soil interactions are also identified by the single-wheel experiments.

The motion profile of the entire rover is numerically evaluated by using a wheel-and-vehicle model in which the wheel-soil model is incorporated into an articulated multibody model for describing the motion dynamics of the vehicle's body and chassis. In the numerical simulation, at first, the traction forces for all the wheels in the longitudinal and lateral directions are computed for certain slip and sinkage conditions. Subsequently, these forces are considered in the forward dynamics procedure to evaluate the accelerations of all the components of the vehicle, which are then numerically integrated to obtain the positions and velocities. The positions of the wheels are used to update the sinkage condition for the subsequent time step, and the velocities are used to update the slip ratios and slip angles.

The simulation results obtained with the wheel-and-vehicle model are compared with the results of steering experiments conducted using a four-wheeled rover test bed. The experiments are carried out on the lunar regolith simulant for different steering angles of the wheels. The proposed model demonstrates better accuracy in predicting steering maneuvers as compared to the conventional kinematics-based model in terms of the position (motion trace) and orientation. Using the proposed wheel-and-vehicle model, path-planning issues can be discussed and mobility/trafficability performance of the rovers can be also evaluated statistically.

This paper is organized as follows. The following section, Section 2, describes the models for the wheel-soil contact mechanics. After reviewing the basics of traction mechanics on loose soil, the modeling of the side force is discussed. The single-wheel experiments and numerical simulations are described in Section 3 along with a discussion on the validity of the wheel-soil models considered in this study. In Section 4, the model for the wheel-and-vehicle dynamics and the simulation procedure using the proposed model are elaborated upon. The steering experiments using a rover test bed are addressed in Section 5, and the validity of the proposed model is then discussed. The performance of the proposed model is also compared with the conventional kinematics-based model.

2   Wheel-soil contact model based on the terramechanics approach

The following analysis concerns a rigid wheel rotating on loose soil. A wheel coordinate system is defined using a right-hand frame, as shown in Figure 1; in this system, the longitudinal direction is denoted by x, the lateral direction by y, and the vertical direction
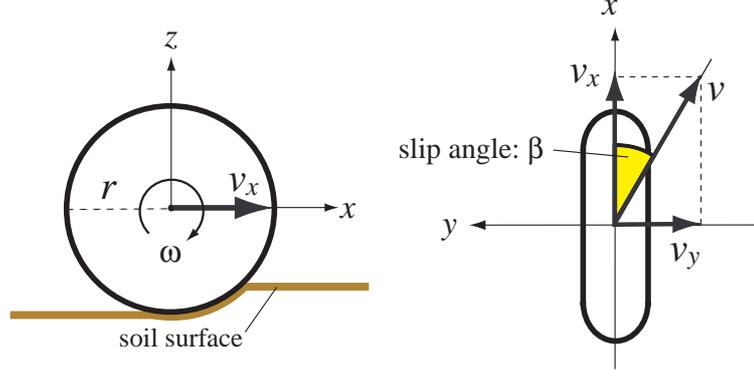
Figure 1: Wheel coordinate system

by z. The coordinate frame rotates according to the steering action of the wheel (the yaw rotation around the z axis) but does not rotate with the driving motion of the wheel (the pitch rotation around the y axis).

2.1 Slip ratio and Slip angle

Slips are generally observed when a rover travels on loose soil. In particular, during steering or slope-traversing maneuvers, slips in the lateral direction are also observed. The slip in the longitudinal direction is expressed by the slip ratio s, which is defined as a function of the longitudinal traveling velocity of the wheel v_x and the circumference velocity of the wheel $r\omega$ (r is the wheel radius and ω represents the angular velocity of the wheel).

$$s = \begin{cases} (r\omega - v_x)/r\omega & (\text{if } |r\omega| > |v_x| : \text{driving}) \\ (r\omega - v_x)/v_x & (\text{if } |r\omega| < |v_x| : \text{braking}) \end{cases} \tag{1}$$

The slip ratio assumes a value in the range from -1 to 1.

On the other hand, the slip in the lateral direction is expressed by the slip angle β, which is defined by using v_x and the lateral traveling velocity v_y as follows:

$$\beta = \tan^{-1}(v_y/v_x) \tag{2}$$

2.2 Wheel sinkage

On loose soil, a wheel has a certain amount of sinkage. The wheel sinkage is divided into static and dynamic sinkages. The static sinkage depends on the vertical load of the wheel, while the dynamic sinkage is caused by the wheel rotation.

According to the equation formulated by Bekker (Bekker, 1960), the static stress $p(h)$ generated under a flat plate, which has a sinkage h and width b, is calculated as follows:

$$p(h) = (k_c/b + k_\phi)\, h^n \tag{3}$$

where k_c and k_ϕ represent pressure-sinkage modules, and n is the sinkage exponent. As shown in Figure 2, by employing equation (3) for a wheel, the following formulae can be
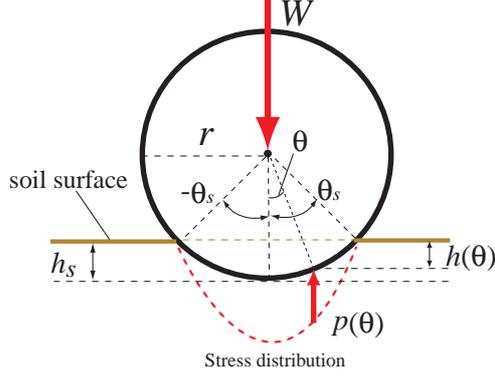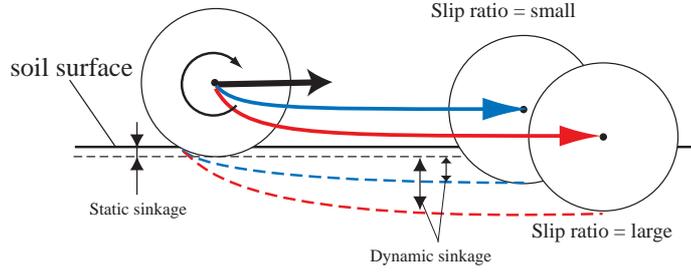
Figure 2: Static sinkage

Figure 3: Dynamic sinkage

derived; First, the wheel sinkage $h(\theta)$ at an arbitrary wheel angle θ is geometrically given by the following:

$$h(\theta) = r(\cos\theta - \cos\theta_s) \qquad (4)$$

where, θ_s is the static contact angle. Subsequently, by substituting equation (4) into equation (3), we obtain the following:

$$p(\theta) = r^n \left(k_c/b + k_\phi\right) \left(\cos\theta - \cos\theta_s\right)^n \qquad (5)$$

The static contact angle θ_s is numerically obtained by solving the following equation when the vertical load of the wheel W is provided:

$$W = \int_{-\theta_s}^{\theta_s} p(\theta) b r \cos\theta d\theta = r^{n+1} \left(k_c + k_\phi b\right) \int_{-\theta_s}^{\theta_s} \left(\cos\theta - \cos\theta_s\right)^n \cos\theta d\theta \qquad (6)$$

Finally, the static sinkage h_s is derived as follows:

$$h_s = r(1 - \cos\theta_s) \qquad (7)$$

On the other hand, as illustrated in Figure 3, the dynamic sinkage is a complicated function depending on the slip ratio of the wheel, the wheel surface pattern, and the soil characteristics. Although it is difficult to obtain an analytical solution for the dynamic sinkage, it is possible to calculate it numerically. In our approach, the dynamic sinkage is numerically evaluated to satisfy the condition $W = F_z$, where F_z represents the vertical force obtained from equation (19) (as shown later). The vertical force acting in the direction from the soil
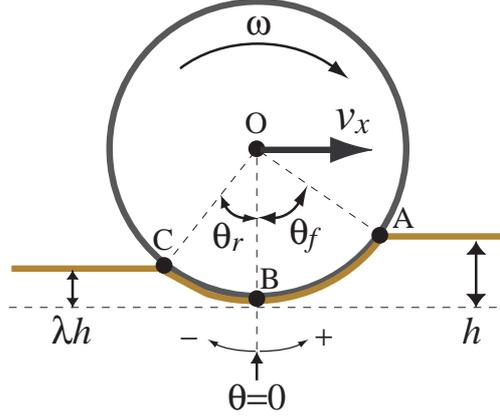
Figure 4: Wheel contact angle

to the wheel is equivalent to the summation of the soil bearing stresses generated at the area of the wheel contact patch. Therefore, F_z increases with the wheel sinkage (or the contact area of the wheel) because the wheel continues to sink if F_z at a wheel sinkage is smaller than a constant W; however, it saturates at a certain amount of wheel sinkage at which the vertical force balances W, and then, F_z never exceed W. This numerical procedure is summarized in Section 3.2.

2.3 Wheel contact angle

Once the wheel sinkage is obtained, the wheel contact angles can be calculated. One of the wheel contact angles is the entry angle and the other is the exit angle. The angle from the vertical to where the wheel initially makes contact with the soil (∠AOB in Figure 4) is defined as the entry angle. The angle from the vertical to where the wheel departs from the soil (∠BOC in Figure 4) is the exit angle. The wheel contact patch on loose soil is defined by the region from the entry angle to the exit angle.

As shown in Figure 4, the entry angle θ_f is expressed as a function of h:
$$\theta_f = \cos^{-1}(1 - h/r) \tag{8}$$

The exit angle θ_r is modeled by using the wheel sinkage ratio λ, which denotes the ratio between the front and the rear sinkages of the wheel.
$$\theta_r = \cos^{-1}(1 - \lambda h/r) \tag{9}$$

The value of λ depends on the soil characteristics, wheel surface pattern, and slip ratio. It decreases below 1.0 when soil compaction occurs, but can be greater than 1.0 when the soil is dug by the wheel and transported to the region behind the wheel.

2.4 Wheel stress distribution

Based on terramechanics models, the stresses under a rotating wheel can be modeled as shown in Figure 5.

The normal stress $\sigma(\theta)$ is determined by the following equation (Yoshida et al., 2003):

$$\sigma(\theta) = \begin{cases} r^n \left(\frac{k_c}{b} + k_\phi \right) [\cos\theta - \cos\theta_f]^n & (\theta_m \leq \theta < \theta_f) \\ r^n \left(\frac{k_c}{b} + k_\phi \right) \left[\cos\{\theta_f - \frac{\theta-\theta_r}{\theta_m-\theta_r}(\theta_f - \theta_m)\} - \cos\theta_f \right]^n & (\theta_r < \theta \leq \theta_m) \end{cases} \tag{10}$$

Note that the above equation is based on Bekker's formula, described in equation (3), and it is merged with the model reported in (Wong and Reece, 1967) to approximate their experimental results. In addition, our model and the Wong-Reece model for the normal stress become equivalent when $n = 1$.

Further, θ_m is the specific wheel angle at which the normal stress is maximized:

$$\theta_m = (a_0 + a_1 s)\theta_f \tag{11}$$

where a_0 and a_1 are parameters that depend on the wheel-soil interaction. Their values are generally assumed as $a_0 \approx 0.4$ and $0 \leq a_1 \leq 0.3$ (Wong and Reece, 1967).

The shear stresses $\tau_x(\theta)$ and $\tau_y(\theta)$ are expressed using identical expressions (Janosi and Hanamoto, 1961):

$$\tau_x(\theta) = (c + \sigma(\theta)\tan\phi)[1 - e^{-j_x(\theta)/k_x}] \tag{12}$$

$$\tau_y(\theta) = (c + \sigma(\theta)\tan\phi)[1 - e^{-j_y(\theta)/k_y}] \tag{13}$$

In these equations, c represents the cohesion stress of the soil; ϕ, the internal friction angle of the soil; and k_x and k_y, the shear deformation modules.

Further, j_x and j_y, which are the soil deformations, can be formulated as functions of the wheel angle θ (Wong and Reece, 1967; Yoshida and Ishigami, 2004):

$$j_x(\theta) = r[\theta_f - \theta - (1 - s)(\sin\theta_f - \sin\theta)] \tag{14}$$

$$j_y(\theta) = r(1 - s)(\theta_f - \theta) \cdot \tan\beta \tag{15}$$

2.5 Drawbar pull : F_x

A general force model for a rigid wheel on loose soil is presented in Figure 6. Using the normal stress $\sigma(\theta)$ and the shear stress in the x direction $\tau_x(\theta)$, the drawbars pull F_x, which acts in the direction from the soil toward the wheel, is calculated by integrating from the entry angle θ_f to the exit angle θ_r (Wong and Reece, 1967):

$$F_x = rb \int_{\theta_r}^{\theta_f} \{\tau_x(\theta)\cos\theta - \sigma(\theta)\sin\theta\}d\theta \tag{16}$$

2.6 Side force : F_y

The side force F_y acts along the lateral direction of a wheel when the vehicle makes a steering maneuver. We model the side force as follows (Yoshida and Ishigami, 2004):
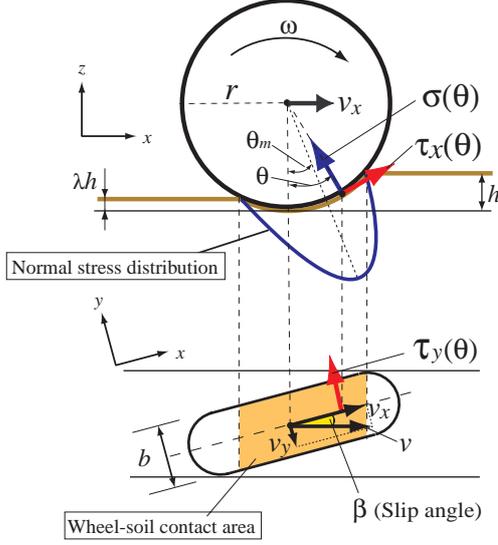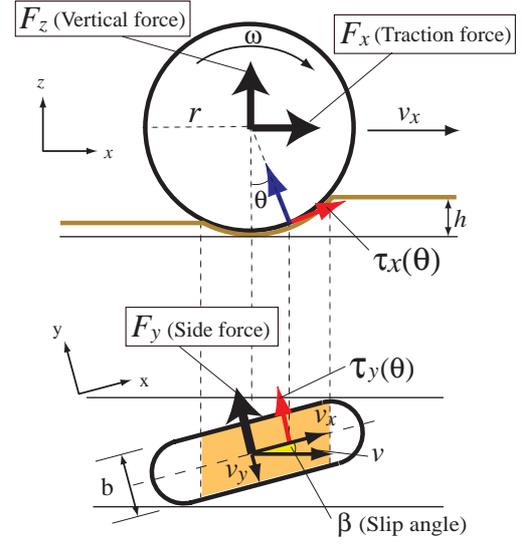
$$F_y = F_u + F_s$$

Figure 5: Wheel stress model

Figure 6: Wheel force model

As shown in Figures 6 and 7, F_u is the force produced by $\tau_y(\theta)$ beneath the wheel, while F_s is the reaction force generated by the bulldozing phenomenon on a side face of the wheel. Then, the above equation can be rewritten as follows:

$$F_y = \int_{\theta_r}^{\theta_f} \{\underbrace{rb \cdot \tau_y(\theta)}_{F_u} + \underbrace{R_b \cdot (r - h(\theta)\cos\theta)}_{F_s}\}d\theta \tag{17}$$

We applied *Hegedus' bulldozing resistance estimation* (Hegedus, 1960) in order to derive the force F_s. As shown in Figure 8, a bulldozing resistance R_b is generated per unit width of a blade when the blade moves toward the soil. According to Hegedus' theory, the bulldozed area is defined by a destructive phase which is modeled by a planar surface. In the case of a horizontally placed wheel, the angle of approach α' should be zero. Then, R_b can be calculated as a function of $h(\theta)$ as follows:

$$R_b(h) = D_1\left(c \cdot h(\theta) + D_2 \cdot \frac{\rho_d \cdot h^2(\theta)}{2}\right) \tag{18}$$

where,

$$
\begin{aligned}
D_1(X_c, \phi) &= \cot X_c + \tan(X_c + \phi) \\
D_2(X_c, \phi) &= \cot X_c + \cot^2 X_c / \cot \phi
\end{aligned}
$$

In the above equations, ρ_d represents the soil density. Further, based on Bekker's theory (Bekker, 1960), the destructive angle X_c can be approximated as follows:
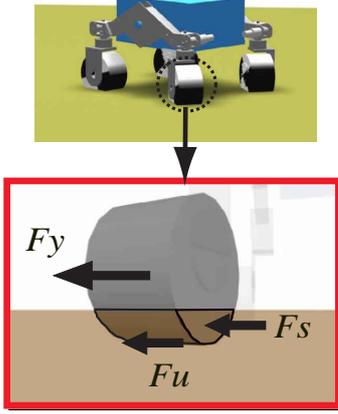
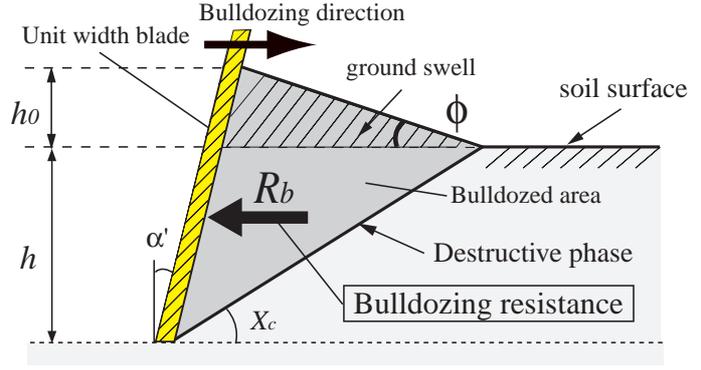$$X_c = 45° - \phi/2$$

Figure 7: Side forces acting on the wheel

Figure 8: Estimation model of the bulldozing resistance

2.7 Vertical force : F_z

The vertical force should be equal to the normal load of the wheel. The vertical force F_z is obtained by the same method as described in equation (16) (Wong and Reece, 1967):

$$F_z = rb \int_{\theta_r}^{\theta_f} \{\tau_x(\theta) \sin \theta + \sigma(\theta) \cos \theta\} d\theta \qquad (19)$$

3 Single-wheel experiments and discussion

To validate the wheel-soil contact model, experiments using a single-wheel test bed were conducted. The experimental results were compared with the numerical simulation results obtained from the wheel-soil contact model. In particular, the characteristics of both the drawbar pull and the side force were confirmed.

3.1 Single-wheel test bed

Figure 9 shows the overview and schematic view of the single-wheel test bed. The test bed comprises both a conveyance unit and a wheel-driving unit. The steering angle (which is equivalent to the slip angle in this test bed) is set between the conveyance unit and the wheel. The translational velocity and angular velocity of the wheel are calculated based on the data obtained by the encoders that are mounted on the conveyance motor and wheel-driving motor, respectively. The forces and torques generated by the wheel locomotion are measured using a six-axis force/torque sensor located between the steering part and the wheel. The wheel sinkage is measured by using a linear potentiometer. A wheel with a diameter of 0.18 [m] and a width of 0.11 [m] is covered with paddles having heights of 0.01 [m]. The load of the wheel is approximately 6.6 [kg].

The vessel of the single-wheel test bed is filled with 12 [cm] (depth) of loose soil, *lunar regolith simulant* which is equivalent to *FJS-1* (Kanamori et al., 1998). The simulated lunar

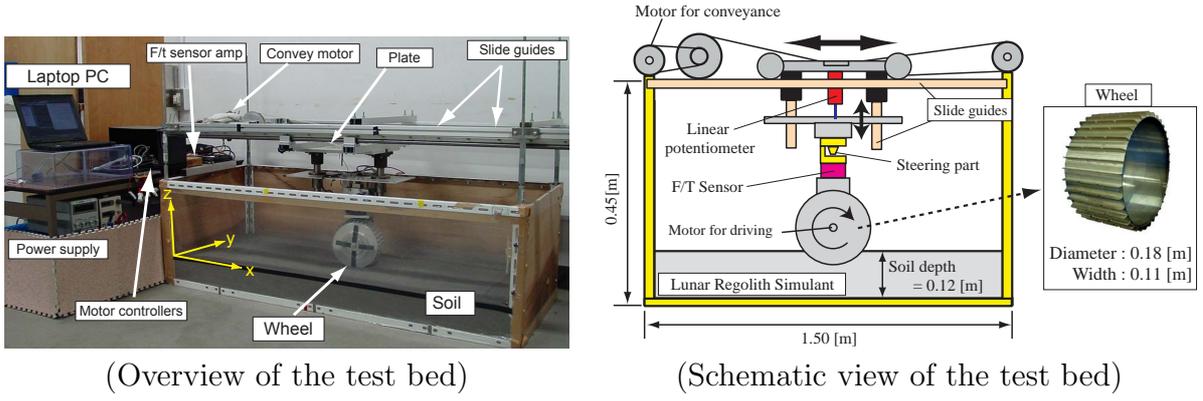(Overview of the test bed)   (Schematic view of the test bed)

Figure 9: Single-wheel test bed

soil consists of material components and mechanical characteristics similar to those of the real lunar soil, as reported in (Heiken et al., 1991).

In the following experiments, the wheel is made to rotate with a controlled constant velocity (0.030 [m/s]) by the driving motor, which is mounted inside the wheel. The translational velocity of the wheel is also controlled such that the slip ratio of the wheel is set from 0.0 to 0.8 in steps of 0.1. The slip ratio is constant during each run. Further, the value of the slip angle of the wheel is varied from 5° to 30° in steps of 5°. Multiple test runs were conducted for a single set of the abovementioned conditions; the total number of runs was more than 100. In addition, during each run, more than 100 data points were extracted for the analysis.

3.2 Numerical simulation procedure

The simulations using the wheel-soil contact model were performed under the same conditions as those of the single-wheel experiments. The parameters used in the simulations are listed in Table 1. Each parameter is experimentally determined by the following methods: c and ϕ (or X_c) are determined by the shear strength test (Bekker, 1960), and k_c, k_ϕ, and n are measured by the pressure-sinkage relationship test (Bekker, 1960). The wheel sinkage ratio λ is visually estimated by measuring the average heights in both the front and rear regions of the wheel. The shear deformation modules, k_x and k_y, are empirically estimated as functions of the slip angle β. Note that every parameter is assumed to independent of gravity, and the terrain in the simulation is assumed to be homogenous.

The simulation model described in Figure 10 is completely equivalent to the single-wheel test bed.

The procedure for the numerical simulation to obtain the wheel forces (drawbar pull and side force) is summarized as follows:

1. Input the normal load W of the wheel, slip ratio s, and slip angle β. (these values are maintained constant during the following procedure.)
2. Calculate the wheel sinkage h from the relationship between W and F_z.

Table 1: Simulation parameters and values

parameter	value	unit	description
c	0.80	[kPa]	cohesion stress
ϕ	37.2	[deg]	friction angle
X_c	26.4	[deg]	soil distractive angle
k_c	1.37×10^3	[N/m^{n+1}]	pressure-sinkage module
k_ϕ	8.14×10^5	[N/m^{n+2}]	pressure-sinkage module
n	1.00		sinkage exponent
a_0	0.40		
a_1	0.15		
ρ_d	1.6×10^3	[kg/m^3]	soil density
λ	0.90 - 1.10		wheel sinkage ratio
k_x	$0.043 \times \beta + 0.036$	[m]	soil deformation module
k_y	$0.020 \times \beta + 0.013$	[m]	soil deformation module

3. Determine the entry angle θ_f and the exit angle θ_r from h (equations (8) and (9)).

4. Determine the normal stress $\sigma(\theta)$, the shear stresses $\tau_x(\theta)$, and $\tau_y(\theta)$ beneath the wheel (equations (10), (12), and (13)).

5. Determine the drawbar pull F_x, side force F_y, and vertical force F_z by using equations (16), (17), and (19), respectively.

6. If $W \neq F_z$, return to step 2.

3.3   Results and discussions

Experimental measurements of the drawbar pull and side force are plotted with error bars in Figures 11 and 12, respectively, for each slip angle from 5° to 30°. As mentioned above, hundreds of data points were obtained from a single test run. Each plot corresponds to the average value of these data points, and the error bar indicates the standard deviation. The theoretical curves calculated by the wheel-soil contact model are also plotted in these figures.

From Figure 11, it is seen that the drawbar pull increases with the slip ratio. The reason for this behavior is that the soil deformation (shear stress) in the longitudinal direction of the wheel increases with the slip ratio; this results in a large soil deformation which, in turn, generates a large drawbar pull. In the range of slip ratios from 0 to 0.3, the drawbar pull becomes smaller with increasing slip angles. This is because the shearing motion in the longitudinal direction decreases as the lateral slip (slip angle) increases.

The differences between the experimental and theoretical values are relatively small in the range of slip angles from 5°-20°; however, relatively larger differences are observed for larger slip angles ($\geq 25°$). The reason for this is considered that the soil beneath the wheel becomes fluidized and different mechanics may dominate the phenomena in high slip ratio and high slip angle conditions. In practice, however, such large slip angles are rarely experienced
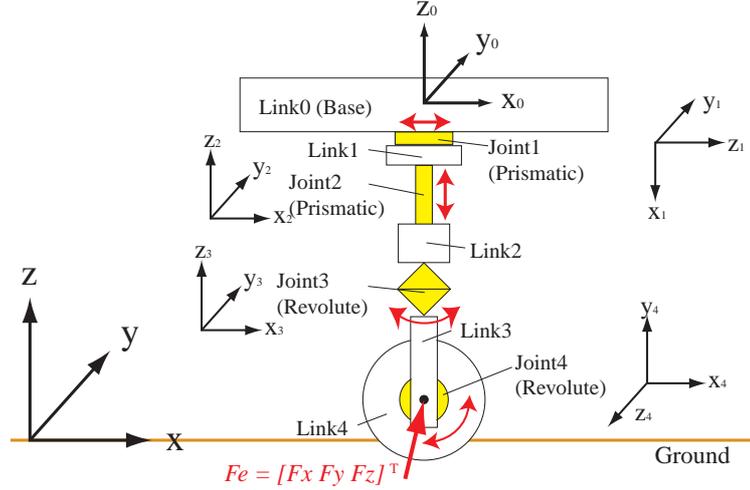
Figure 10: Simulation model for the single-wheel test bed

under normal steering maneuvers.

Figure 12 shows that the side force decreases along with the slip ratio and increases according to the slip angle. The larger the slip angle, the larger is the lateral velocity on the wheel; this leads to a larger side force. In addition, it is observed that the side force has its maximum value at $s = 0.0$; this is because the lateral velocity, in proportion to the longitudinal velocity, is maximized at $s = 0.0$ for each slip angle. The theoretical curves agree well with the plotted experimental results.

These results confirm that the wheel-soil contact model proposed in this paper is able to represent the motion behavior of the wheel and the contact/traction forces with appropriate accuracy.

4 Wheel-and-vehicle model

To describe the motion dynamics of the vehicle's body and chassis, a wheel-and-vehicle model is developed. In this model, the rover is modeled as an articulated body system to calculate the motion dynamics of its body and chassis. Furthermore, the contact forces on each wheel of the rover can be obtained by using the wheel-soil contact model. In this paper, the vehicle model refers to our rover test bed.

4.1 Rover test bed

The four-wheeled rover test bed, shown in Figure 13, has the dimensions 0.68 [m] (length) × 0.44 [m] (width) × 0.32 [m] (height) and weighs approximately 35 [kg] in total. Each wheel has the same configuration as that in the single-wheel experiments. All the wheels have active steering degree of freedom (DOF). The wheels are connected to the main body by a rocker suspension. The rocker is a non spring passive suspension mechanism that connects
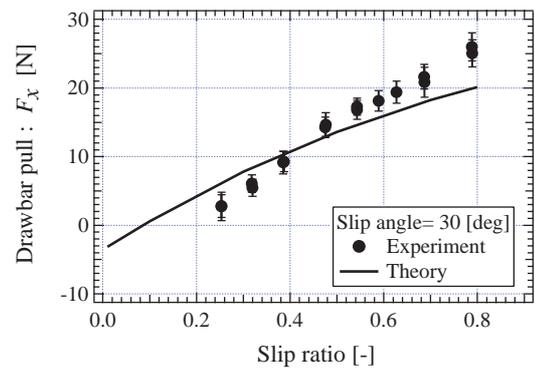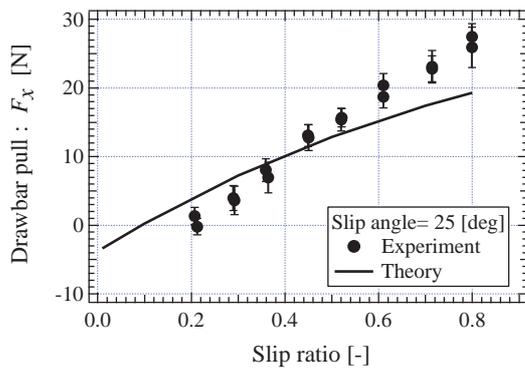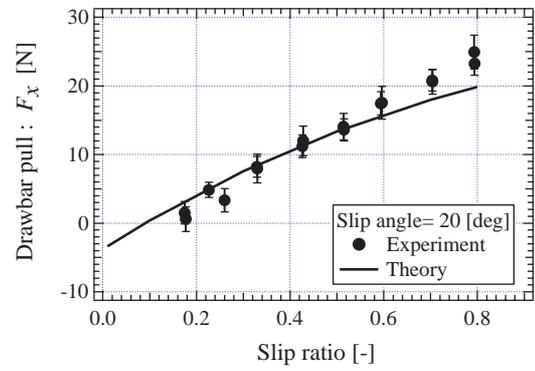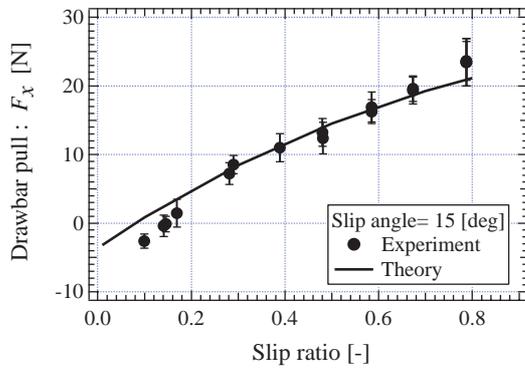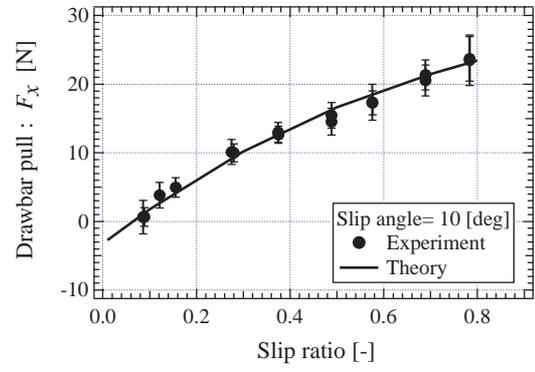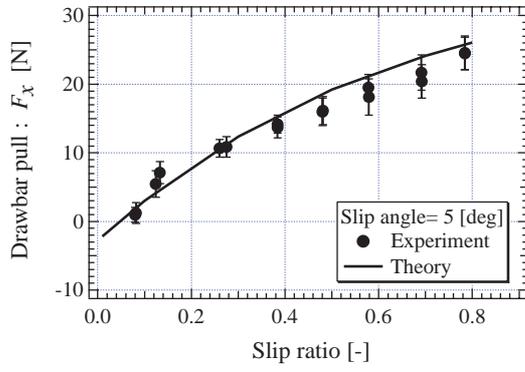
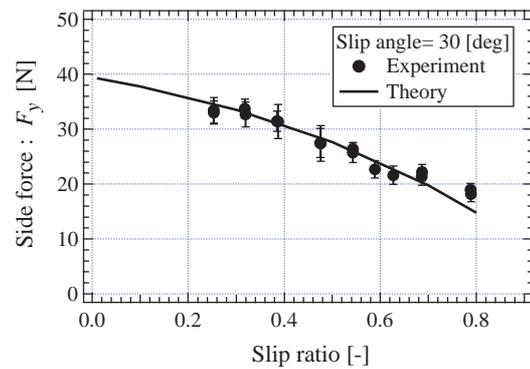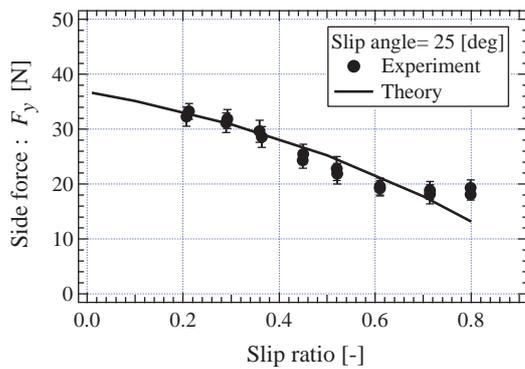Figure 11: Experimental and simulation results (Slip ratio - Drawbar pull)

Slip angle = 5 [deg]

Slip angle = 10 [deg]

Slip angle = 15 [deg]

Slip angle = 20 [deg]
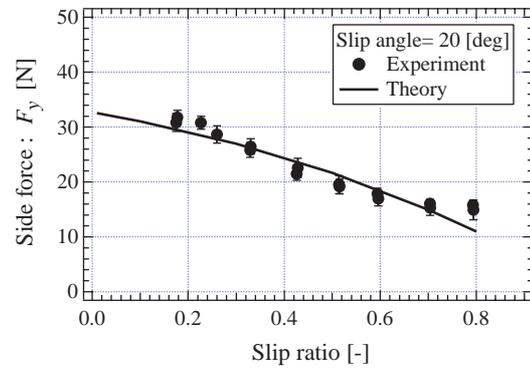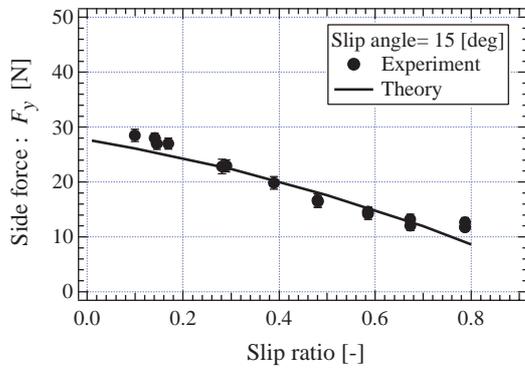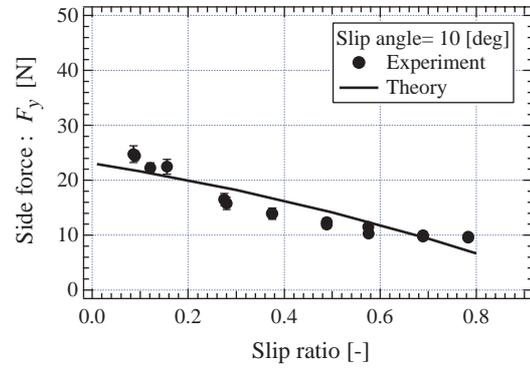
Slip angle = 25 [deg]
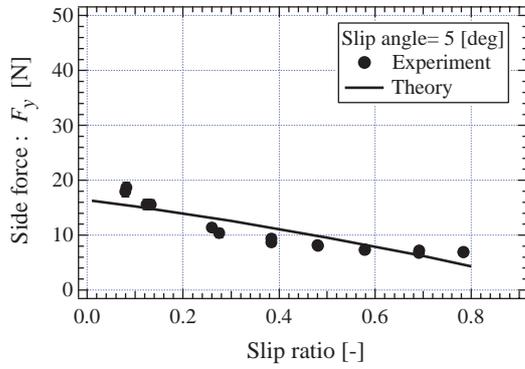
Slip angle = 30 [deg]

Figure 12: Experimental and simulation results (Slip ratio - Side force)
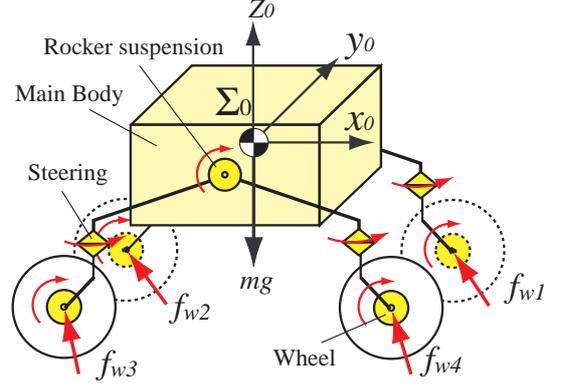
Figure 13: Rover test bed
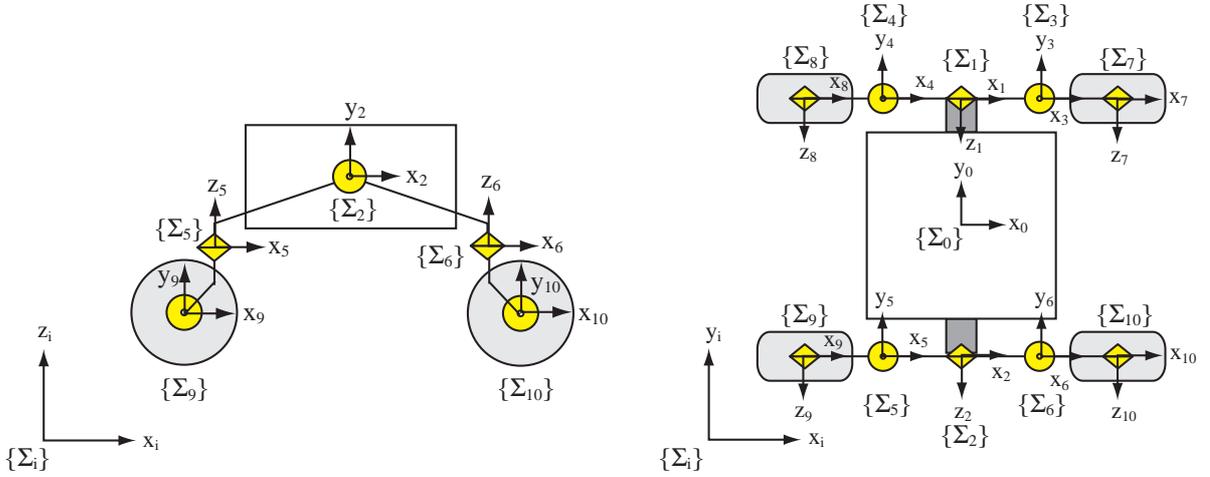

Figure 14: Rover dynamics model

Figure 15: Coordinate system of the rover model

the wheels by free-pivot links. This differential link is used to keep the pitch angle of the main body in the middle of the left and right rocker angles.

4.2   Definition of wheel-and-vehicle model

The dynamics model of the rover shown in Figure 14 is completely equivalent to the rover test bed. The coordinate system of the rover is described in Figure 15. The positions and orientations of the rover are expressed by Euler angles based on an inertial coordinate system $\{\Sigma_i\}$.

The dynamic motion equation of the rover is generally written as:

$$\boldsymbol{H} \begin{bmatrix} \dot{\boldsymbol{v}}_0 \\ \dot{\boldsymbol{\omega}}_0 \\ \ddot{\boldsymbol{q}} \end{bmatrix} + \boldsymbol{C} + \boldsymbol{G} = \begin{bmatrix} \boldsymbol{F}_0 \\ \boldsymbol{N}_0 \\ \boldsymbol{\tau} \end{bmatrix} + \boldsymbol{J}^T \begin{bmatrix} \boldsymbol{F}_e \\ \boldsymbol{N}_e \end{bmatrix} \tag{20}$$

where $\boldsymbol{H}$ represents the inertia matrix of the rover; $\boldsymbol{C}$, the velocity depending term; $\boldsymbol{G}$, the

Table 2: Kinematics parameters of the rover test bed

Coordinate	x axis [m]	y axis [m]	z axis [m]
$\{\Sigma_0\} \rightarrow \{\Sigma_1\}$	0.0	0.172	0.032
$\{\Sigma_0\} \rightarrow \{\Sigma_2\}$	0.0	−0.172	0.032
$\{\Sigma_1\} \rightarrow \{\Sigma_3\}$	0.248	−0.064	0.0
$\{\Sigma_1\} \rightarrow \{\Sigma_4\}$	−0.248	−0.064	0.0
$\{\Sigma_2\} \rightarrow \{\Sigma_5\}$	−0.248	−0.064	0.0
$\{\Sigma_2\} \rightarrow \{\Sigma_6\}$	0.248	−0.064	0.0
$\{\Sigma_3\} \rightarrow \{\Sigma_7\}$	0.0	0.0	−0.195
$\{\Sigma_4\} \rightarrow \{\Sigma_8\}$	0.0	0.0	−0.195
$\{\Sigma_5\} \rightarrow \{\Sigma_9\}$	0.0	0.0	−0.195
$\{\Sigma_6\} \rightarrow \{\Sigma_{10}\}$	0.0	0.0	−0.195

Table 3: Dynamics parameters of the rover test bed

Link name	Link number	Mass [kg]	Inertia [kgm^2]		
			I_x	I_y	I_z
Main body	0	11.02	0.100	0.111	0.138
Rocker arm	1, 2	3.81	0.008	0.146	0.147
Steering block	3 - 6	1.20	0.005	0.005	0.001
Wheel	7 - 10	2.30	0.008	0.008	0.008

gravity term; $\boldsymbol{v}_0$, the translational velocity of the main body; $\boldsymbol{\omega}_0$, the angular velocity of the main body; $\boldsymbol{q}$, the angle of each joint of the rover; $\boldsymbol{F}_0 = [0, 0, 0]^T$, the external forces acting at the centroid of the main body; $\boldsymbol{N}_0 = [0, 0, 0]^T$, the external moments acting at the centroid of the main body; $\boldsymbol{\tau}$, the torques acting at each joint of the rover; $\boldsymbol{J}$, the Jacobian matrix; $\boldsymbol{F}_e = [f_{w1}, \ldots, f_{wm}]$, the external forces acting at the centroid of each wheel; $\boldsymbol{N}_e$, the external moments acting at the centroid of each wheel.

Note that each external (contact) force f_{wi} $(i = 1, \ldots, m)$ is derived by the wheel-soil contact model, as mentioned in Section 2. Here, m denotes the number of wheels. Equation (20) is a general equation and can be applied to a vehicle with any configuration. The steering dynamics of the rover for given traveling and steering conditions are numerically obtained by solving equation (20) successively.

Specific parameters for the kinematics and dynamics of the rover test bed are summarized in Tables 2 and 3, respectively.

4.3   Simulation procedure

The simulation procedure for using the proposed model is summarized as follows:

1. Input the steering angles δ_{wi} and wheel angular velocities ω_{wi} for each wheel ($i =$
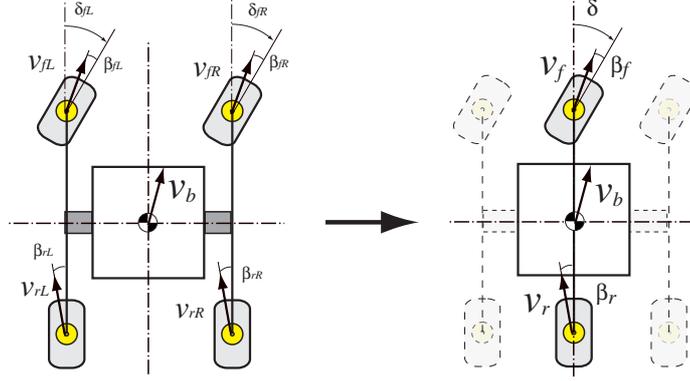
Figure 16: Conventional kinematics-based model : Bicycle model

$1, \ldots, 4$, in this case). These values are the same as those of the experiments.

2. Determine $\boldsymbol{\tau}$ such that the steering and wheel angular velocity inputs are satisfied.

3. Derive the external forces f_{wi} acting at each wheel by using the wheel-soil contact model, and then determine $\boldsymbol{F_e}$ and $\boldsymbol{N_e}$.

4. Solve equation (20) to obtain the rover's positions, orientations, and velocities.

5. Calculate the slip ratios and slip angles of each wheel, and then return to step 3.

The simulation is performed using the *Open Dynamics Engine* (ODE, 2006) to obtain the forward dynamics solution of equation (20).

5   Steering experiments and discussion

The steering experiments were conducted in order to validate the wheel-and-vehicle model. The corresponding dynamics simulations using the proposed model were also carried out and the simulation results were compared to those of the experiments. A conventional kinematics-based model, which is called the *bicycle model* (Shiller and Sunder, 1996), was also compared with the corresponding experiment so as to determine the extent of improvement in the performance of the proposed model. As shown in Figure 16, the bicycle model approximates a four-wheel car-like vehicle as a two-wheel bicycle-like vehicle. In this approximation, the left and right wheels are assumed to have identical characteristics and behaviors. For the modeling of the steering maneuvers of the vehicle, the conventional kinematics-based approach using the bicycle model yields a simple circular arc as a function of the traveling velocity of the vehicle and the steering angle of the wheel. Note that in the bicycle model only the lateral slips of wheels (not the longitudinal slips) are taken into account.

We conducted the following experiments using our rover test bed, as shown in Figure 13. The steering experiments were conducted under different conditions, and a set of typical results are presented in this paper.

Table 4: Experimental conditions

		Case A	Case B
Steering angle [deg]	Front wheels	15.0	30.0
	Rear wheels	0.0	0.0
Wheel angular velocity [rad/s]		0.3 (2.86 [rpm])	
Average traveling velocity [m/s]		0.03	

5.1 Experimental setup and conditions

The test field, which consists of a flat rectangular vessel measuring 1.5×2.0 [m], is evenly filled with 10 [cm] (depth) of the lunar regolith simulant.

The rover test bed travels with a given angular velocity and steering angle. Each wheel is controlled to travel with a constant wheel angular velocity and steering angle by an on-board computer. The steering trajectories of the rover are measured using a 3D optical sensor system fixed on the ceiling. A force/torque sensor is also mounted at the mechanical interface between each wheel assembly and the steering joint to measure the forces generated by the corresponding wheel.

The conditions for two typical cases in the steering experiments are listed in Table 4: in case A, the steering angles of the left and right front wheels were fixed at keep 15°, whereas in case B, they were fixed at 30°. The steering angles of the left and right rear wheels were 0° in both cases. In every experiment, the given angular velocity of each wheel was maintained at 0.3 [rad/s] (2.86 [rpm]). The average traveling velocity of the rover was around 0.03 [m/s]. We repeated the experiments twice for each steering case.

5.2 Results and discussion

Figure 17 shows snapshot pictures of one of the experiments and computer graphics images obtained by the corresponding dynamics simulation.

The experimental results regarding the steering trajectories of the rover are shown in Figures 18 (case A) and 19 (case B). The steering trajectories obtained from both the wheel-and-vehicle model and the conventional kinematics-based model are also plotted in the same figures. In addition, the time histories of the orientation (yaw angle) of the rover in each experiment are shown in Figures 20 and 21.

The errors between the experiments and the simulations are summarized in Tables 5 and 6 along with the position (distance) and orientation (yaw angle) errors. The errors are evaluated by both root mean square (RMS) error and the final state error. The error percentage for the position is calculated by dividing the error value at the final state by the total travel distance, while that for the orientation is determined by dividing the error value by the yaw angle in the final state.
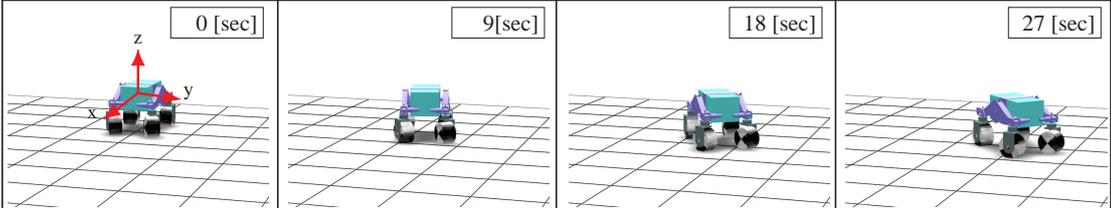
Experiment
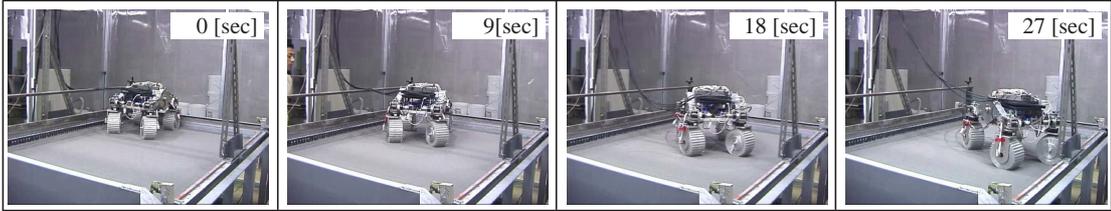
Simulation

Figure 17: Comparison of the simulated and experimental steering motion (case B)

From Figures 18 and 19, the repeatability of the experiments regarding the steering trajectories can be confirmed. It can also be observed that in terms of steering trajectories, the proposed model simulates the experimental results better than the conventional model. Taking into account wheel slippage, the proposed model calculates better steering trajectories, which almost agree with the experimental results. As described in Table 5, the RMS error of the proposed model is negligible (less than 0.04 [m]), while that of the conventional model is greater than 0.13 [m]. The accuracy of the proposed model is better than 0.09 [m] (less than the wheel width) even in the final state. The proposed model simulates the experimental steering trajectories with considerably better accuracy than the conventional model from the viewpoint of the error percentages. Figures 20 and 21 also clearly illustrate that the proposed model exhibits good accuracy in the estimation of the rover orientation.

In summary, the errors of 20%-30% in the position were observed for the conventional kinematics-based model; however, they have been reduced to less than 8%, or one-fifth on average, by the proposed model. Furthermore, the errors of 40%-50% in the orientation have been reduced to less than 15%, or only one-seventh on average, by the proposed model.

Throughout the experiments, it was observed that the slip ratios were in the range from 0.1 to 0.3 and the slip angles were in the range from $-7°$ to $15°$. Despite such dynamic wheel behavior, our model is able to calculate the wheel slippage and the steering motion of the rover with a remarkably improved accuracy.

6   Conclusions and future work

This paper addressed analytical models to investigate the steering maneuvers of planetary exploration rovers. The proposed models have been developed and validated using the following two steps.
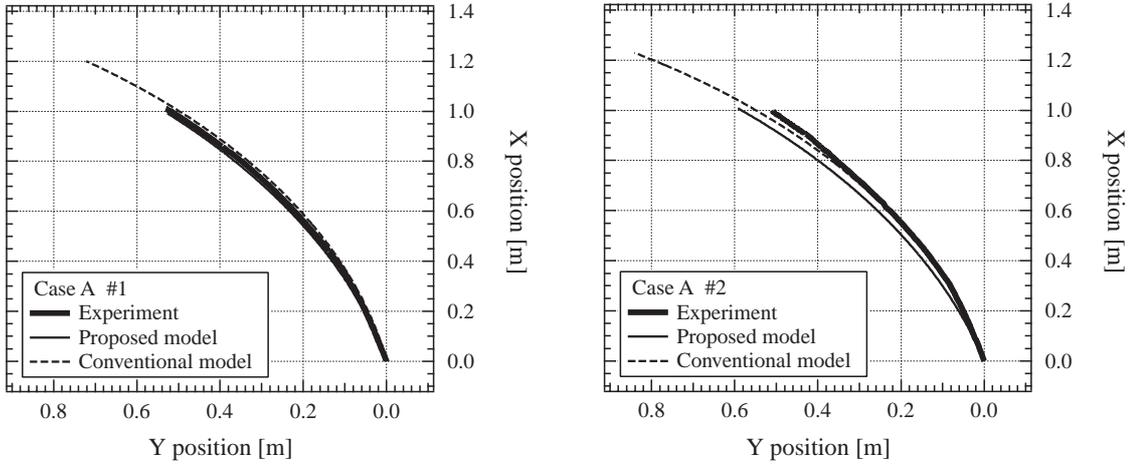
Figure 18: Comparison of the simulated and experimental steering trajectories (case A)
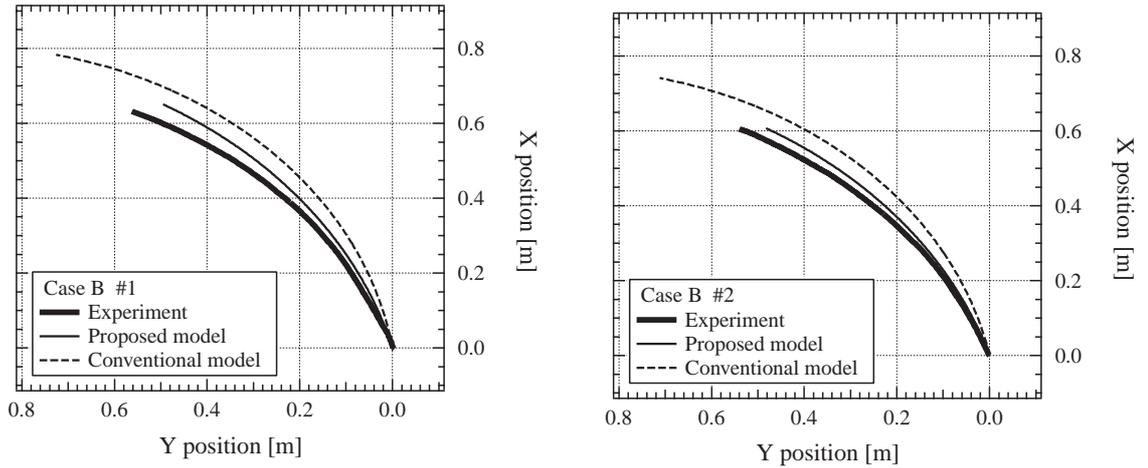

Figure 19: Comparison of the simulated and experimental steering trajectories (case B)

Table 5: RMS and final state errors for the position (distance) error

		Conventional model		Proposed model	
		RMS error	Final state error	RMS error	Final state error
Case A	# 1	0.157	0.269 (22.9%)	0.015	0.019 (1.6%)
	# 2	0.192	0.407 (30.1%)	0.035	0.086 (6.3%)
Case B	# 1	0.139	0.222 (24.8%)	0.039	0.070 (7.8%)
	# 2	0.137	0.219 (23.9%)	0.032	0.056 (6.3%)

(Unit is [m] and percentages for the final state error are in parentheses.)
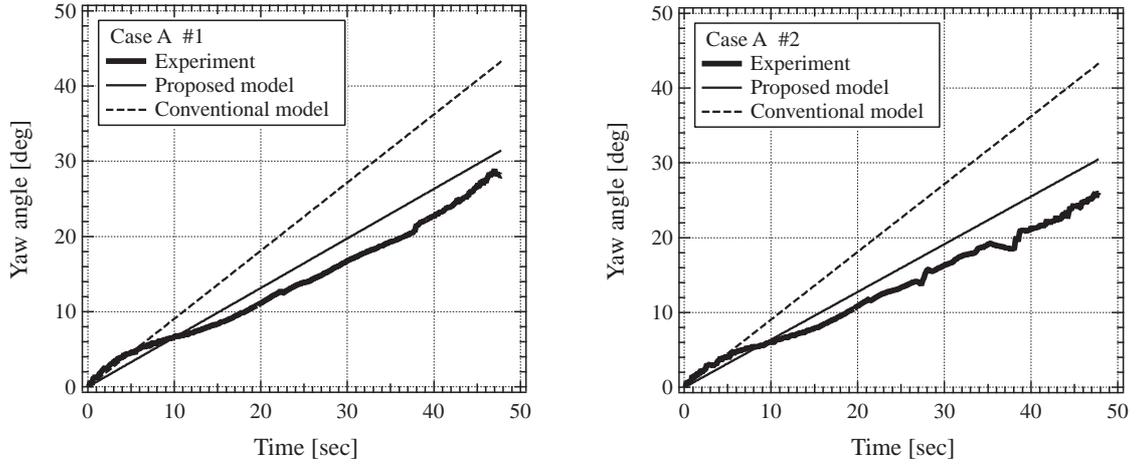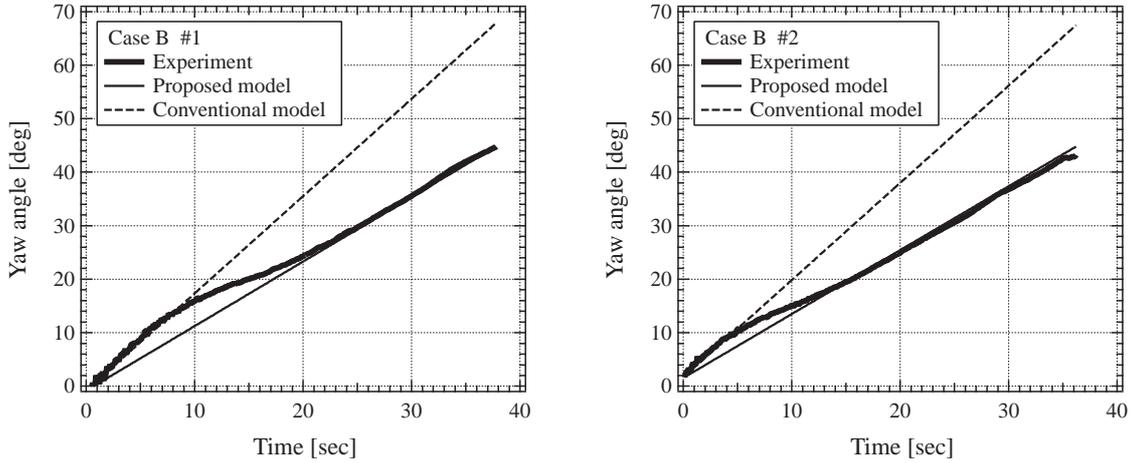
Figure 20: Time history of the yaw angles (case A)

Figure 21: Time history of the yaw angles (case B)

Table 6: RMS and final state errors for the orientation (yaw angle) error

		Conventional model		Proposed model	
		RMS error	Final state error	RMS error	Final state error
Case A	# 1	9.298	15.22 (46.4%)	2.537	3.383 (10.3%)
	# 2	10.92	18.52 (54.0%)	3.062	4.863 (14.2%)
Case B	# 1	12.63	23.12 (51.6%)	2.460	0.001 (0.0%)
	# 2	13.54	24.24 (56.1%)	1.332	1.558 (3.6%)

(Unit is [deg] and percentages for the final state error are in parentheses.)

In the first step, the wheel-soil contact model, which can calculate the three-axis forces of the wheel on loose soil, has been elaborated upon based on terramechanic analyses. In particular, the modeling of the side force has been developed by considering the shear forces beneath the wheel and the bulldozing resistance on the side face of the wheel. Through the single-wheel experiments using the simulated lunar soil, it is confirmed that the wheel-soil contact model agrees well with the experimental results. The mechanics of the traction forces are characterized as follows. The drawbar pull, which is the net traction force in the longitudinal direction, increases with increasing slip ratios and decreases with increasing slip angles. On the other hand, the side force, which is the net traction force in the lateral direction, increases with increasing slip angles and decreases with increasing slip ratios.

In the second step, the wheel-and-vehicle model, which considers both the longitudinal and lateral forces exerted on all the wheels, has been developed for a better analysis of the steering maneuvers of the vehicle. In this model, the rover is modeled as an articulated multibody system in order to calculate the motion dynamics of the rover's body and chassis. In the numerical simulation, the contact/traction forces on each wheel are evaluated by the wheel-soil model developed in the above step for the slip conditions at each moment; subsequently, these forces are incorporated into the forward dynamics computation to obtain the motion of the vehicle. Through the steering experiments using a four-wheel rover test bed on the simulated lunar soil, it has been confirmed that the proposed model provides better accuracy in evaluating the steering trajectory as compared to the conventional kinematics-based model, which is termed the bicycle model.

The main contributions of this paper are summarized in the following three points.

- Three-axis forces, drawbar pull, side force, and vertical force of a rigid wheel on loose soil were systematically modeled based on the terramechanics analyses, and the validity of the model was evaluated by experiments using the simulated lunar soil.

- The characteristics of the drawbar pull and side force for different slip/skid conditions of the wheel were thoroughly discussed. The proposed model is adequate for a qualitative understanding of the slip/skid behavior as well as a quantitative evaluation of the traction forces of the wheel.

- The wheel-and-vehicle model was developed to simulate the steering motion of the rover by combining the terramechanics-based wheel model and the dynamics-based vehicle model. It was confirmed that the model performs with better accuracy in predicting the steering maneuvers of a vehicle on loose soil.

The models developed in this paper are useful in performing off-line computation of the vehicle motion trajectories under slipping/skidding conditions. Such computation is important for path planning issues. In the planning phase, appropriate maneuvers should be planned to increase the performance or to decrease the hazards to the vehicle. Tip-over is one of the fatal hazards, and immobility due to a wheel-stuck in very soft soil is considered to be another hazard. Path planning with the criterion of minimum slippage can be discussed using the proposed models. The discussion can also be extended to evaluate the performance of the vehicle's climbing/traversing capabilities because the slope climbing performance is limited by the mobility of the wheels.

Furthermore, the proposed methods can be extended to on-line applications, such as controlling the driving/steering motion of the vehicle to follow a given path by compensating for the wheel slippages. Such control could be realized by accelerating the computation of the dynamics equations presented in this paper.

In this study, we assumed that the terrain was homogenous and the soil parameters were always constant. However, in a real situation, these assumptions are not valid. For uneven terrain with consistent soil parameters, the proposed models and methods are directly applied using an appropriate surface geometry model. However, in case the soil mechanics varies from one place to another, it will be necessary to update the soil and traction parameters according to the variations in the terrain parameters. One possible direction for future research is the on-line determination of these parameters. Sensitivity analysis of the traction forces or the rover performance against variations in the soil parameters should also be considered as another subject for future studies.

References

Bekker, M. G. (1960). *Off-The-Road Locomotion.* Ann Arbor, MI, USA, The University of Michigan Press.

Bekker, M. G. (1969). *Introduction to Terrain-Vehicle Systems.* Ann Arbor, MI, USA, The University of Michigan Press.

Gibbesch, A. and Schäfer, B. (2005). Multibody system modelling and simulation of planetary rover mobility on soft terrain. In *Proceedings of the 8th Int. Symp. on Artificial Intelligence, Robotics and Automation in Space (iSAIRAS '05)*, Munich, GERMANY.

Hegedus, E. (1960). A simplified method for the determination of bulldozing resistance. *Land Locomotion Research Laboratory, Army Tank Automotive Command Report*, 61.

Heiken, G., Vaniman, D., French, B. M., and Schmitt, J. (1991). *Lunar Sourcebook: A User's Guide to the Moon.* Cambridge University Press,.

Iagnemma, K. and Dubowsky, S. (2004). *Mobile Robots in Rough Terrain : Estimation, Motion Planning, and Control with Application to Planetary Rovers (Springer Tracts in Advanced Robotics 12).* Germany, Springer.

Jain, A., Guineau, J., Lim, C., Lincoln, W., Pomerantz, M., Sohl, G., and Steele, R. (2003). Roams: Planetary surface rover simulation environment. In *Proceedings of the 7th Int. Symp. on Artificial Intelligence, Robotics and Automation in Space (iSAIRAS '03)*, Nara, JAPAN.

Janosi, Z. and Hanamoto, B. (1961). The analytical determination of drawbar pull as a function of slip for tracked vehicle in deformable soils. In *Proceedings of the 1st Int. Conf. on Terrain-Vehicle Systems*, Torino, Italy.

Kanamori, H., Udagawa, S., Yoshida, T., Matsumoto, S., and Takagi, K. (1998). Properties of lunar soil simulant manufactured in japan. In *Proceedings of the 6th Int. Conf. and Exposition on Engineering, Construction, and Operations in Space*, Albuquerque, NM, USA.

ODE (2006). Retrieved May 31, 2006, from http://www.ode.org/.

Shiller, Z. and Sunder, S. (1996). Emergency maneuvers of autonomous vehicles. In *Proceedings of the Int. Federation of Automatic Control, and Operations in Space*, San Francisco, CA, USA.

Wong, J. Y. (1978). *Theory of Ground Vehicles*. John Wiley & Sons.

Wong, J. Y. and Reece, A. (1967). Prediction of rigid wheel prefoemance based on the analysis of soil-wheel stresses part i, preformance of driven rigid wheels. *Journal of Terramechanics*, 4:81–98.

Yoshida, K. and Hamano, H. (2002). Motion dynamics of a rover with slip-based traction model. In *Proceedings of the 2002 IEEE Int. Conf. on Robotics and Automation (ICRA '02)*, Washington, DC, USA.

Yoshida, K. and Ishigami, G. (2004). Steering characteristics of a rigid wheel for exploration on loose soil. In *Proceedings of the 2004 IEEE Int. Conf. on Intelligent Robots and Systems (IROS '04)*, Sendai, JAPAN.

Yoshida, K., Watanabe, T., Mizuno, N., and Ishigami, G. (2003). Terramechanics-based analysis and traction control of a lunar/planetary rover. In *Proceedings of the Int. Conf. on Field and Service Robotics (FSR '03)*, Yamanashi, JAPAN.